Natural Hazards (2025) 121:7051–7076
https://doi.org/10.1007/s11069-024-07016-y

ORIGINAL PAPER

Stereo vision from space to track tree fall incident

Sara Alibakhshi[1] · Ruben Valbuena[2] · Daniel Heinlein[3] · Lauri Häme[4] · Petri Pellikka[1,5,6]

Received: 15 March 2024 / Accepted: 6 November 2024 / Published online: 18 December 2024

Abstract

Forests are essential for regulating the climate, enhancement of air quality, and the preservation of biodiversity. However, tree falls pose significant risks to infrastructure, particularly powerlines, leading to widespread blackouts and substantial damage. Traditional methods for monitoring tree fall risks, such as field surveys, are often costly, time-consuming, and lack real-time capabilities. While airborne Light Detection and Ranging (LiDAR) provides precise data for monitoring tree fall risks, it still faces challenges related to frequency of data acquisition and high costs. In response to the European Space Agency's call for more cost-effective monitoring approaches, this study investigates the potential of using very high-resolution optical satellite data, specifically from Pléiades satellite imagery, for assessing tree fall risks to powerlines. Key forest structure metrics such as canopy complexity using the Rumple Index, canopy height, as well as distance to powerlines were analyzed across four study sites in Finland and Switzerland. Sites with simpler canopy structures exhibited stronger correlations between stereo and LiDAR height measurements (R^2 values up to 0.64). Stereo-based measurements can overall provide acceptable accuracy (ca. 96.57%) in detecting trees compared with LiDAR data. The results demonstrated that the Rumple Index can identify areas with simpler canopy structures, where stereo-based height measurements yield high accuracy. These findings suggest the potential of hybrid approaches that integrate both stereo imagery and airborne LiDAR data, tailored to site-specific characteristics, for accurate risk assessments. This study contributes to the ongoing efforts in developing an understanding of vegetation management along powerlines, to inform decision-makers in their endeavors to identify and mitigate risks associated with tree falls.

Keywords Tree fall · Canopy height estimation · Pléiades · Airborne LiDAR · Sentinel-2 · Rumple Index

1 Introduction

Forests are essential for regulating the climate, enhancement of air quality, and the preservation of biodiversity (Brockerhoff et al. 2017; Mooney et al. 2009; Mori et al. 2017). Although forests provide numerous ecosystem services (Akbari et al. 2001; Alvey 2006), tree falls can pose risks to various types of infrastructure such as powerlines (Guggenmoos 2003; Ituen

Extended author information available on the last page of the article et al. 2008). The risk of tree falls on powerlines presents a hazardous threat to power transmission systems, and causes substantial economic damage (Farmer and Allen 2006; Poulos and Camp 2011). To address this issue, the development of efficient methods for monitoring and managing tree fall risk is crucial (Jinqiu et al. 2021; Louit et al. 2009; Sittithumwat et al. 2004).

Traditional methods of monitoring trees that pose a risk to powerlines typically involve field surveys to remove dangerous trees (Poulos and Camp 2011). However, this approach has proven to be expensive, time-consuming, and often lacks timely detection capabilities on a large scale (Ituen and Sohn 2010). Airborne laser scanning based on Light Detection and Ranging (LiDAR) sensors offers promising avenues for assessing the risk of tree-related damage compared with traditional methods (Guan et al. 2021; Ituen et al. 2008; Salas 2021; Wedagedara et al. 2023). However, the use of airborne LiDAR still faces several challenges when it comes to monitoring dangerous trees. Firstly, airborne LiDAR data acquisition is usually conducted infrequently, which limits its ability to provide timely monitoring, despite the need for real-time information (Ahmad et al. 2013). Secondly, airborne LiDAR data acquisition tends to be financially costly compared to satellite, needing specialized equipment and personnel involved in large-scale monitoring projects.

Given the rising concerns regarding the risks of tree falls, this study focuses on assessing where tree falls may cause danger for infrastructures such as powerlines, responding to the European Space Agency's call to find more cost-efficient approaches for monitoring the risks posed by trees. Here, we used Pléiades satellite data to obtain stereo images with spatial resolutions in the sub-meter range across the four sites in Finland and Switzerland (Hobi and Ginzler 2012; Loghin et al. 2020; Piermattei et al. 2018; Wang et al. 2023; Ye et al. 2021). In the stereoscopy technique, by acquiring two or more overlapping images from slightly different perspectives, three-dimensional information to calculate canopy height can be calculated (De Franchis et al. 2014a, d). Numerous studies have demonstrated the feasibility of using very high-resolution optical satellite data for canopy height estimation (Stone et al. 2016). Nevertheless, the accuracy of canopy height estimation using stereo-based height measurements via optical satellite data, which is essential for monitoring the risk of tree fall, exhibits a wide range of values, varying from relatively weak (Lin et al. 2020; Persson et al. 2013; St-Onge et al. 2008; Ullah et al. 2020) to strong performance reported (Breaban et al. 2022; Tong et al. 2012; Ye et al. 2021). The research questions of this study include: (1) can very high-resolution optical satellite data effectively replace airborne LiDAR as a reliable alternative for accurately monitoring tree fall risks? and (2) in which situation optical satellite data can be used to assess tree fall risks?

This study aims to assess whether tree falls, regardless of their cause, could result in damage to powerlines. The approach utilizes stereo-based techniques derived from optical satellite images. We will mainly focus on monitoring tree-related powerline damage risk by estimating key parameters such as canopy height, canopy complexity using the Rumple Index, and tree-to-powerline distance, and provide the comparison between the results of very high-resolution optical data and airborne LiDAR. This study contributes to the ongoing efforts in developing an understanding of vegetation management along powerlines, to inform decision-makers in their endeavors to identify and mitigate risks associated with tree falls.

2 Material and method

2.1 Overview

The flow diagram in Fig. 1 depicts the key procedural steps employed in this study. We first obtained and preprocessed Pléiades stereo images (Sect. 2.3.1) and employed the Satellite Stereo Pipeline (S2P) method to calculate canopy height using optical data (Sect. 2.4.1). Additionally, we obtained airborne LiDAR data (Sect. 2.3.2) to estimate canopy height and tree crown characteristics (Fig. 1, Sect. 2.4.2). We obtained ancillary data (Sect. 2.3.3) by obtaining land cover map using the European Space Agency (ESA) land cover map, Normalized Difference Vegetation Index (NDVI) maps using the Sentinel-2 data and the Rumple Index maps using airborne LiDAR data (Sect. 2.4.3). By integrating the layers

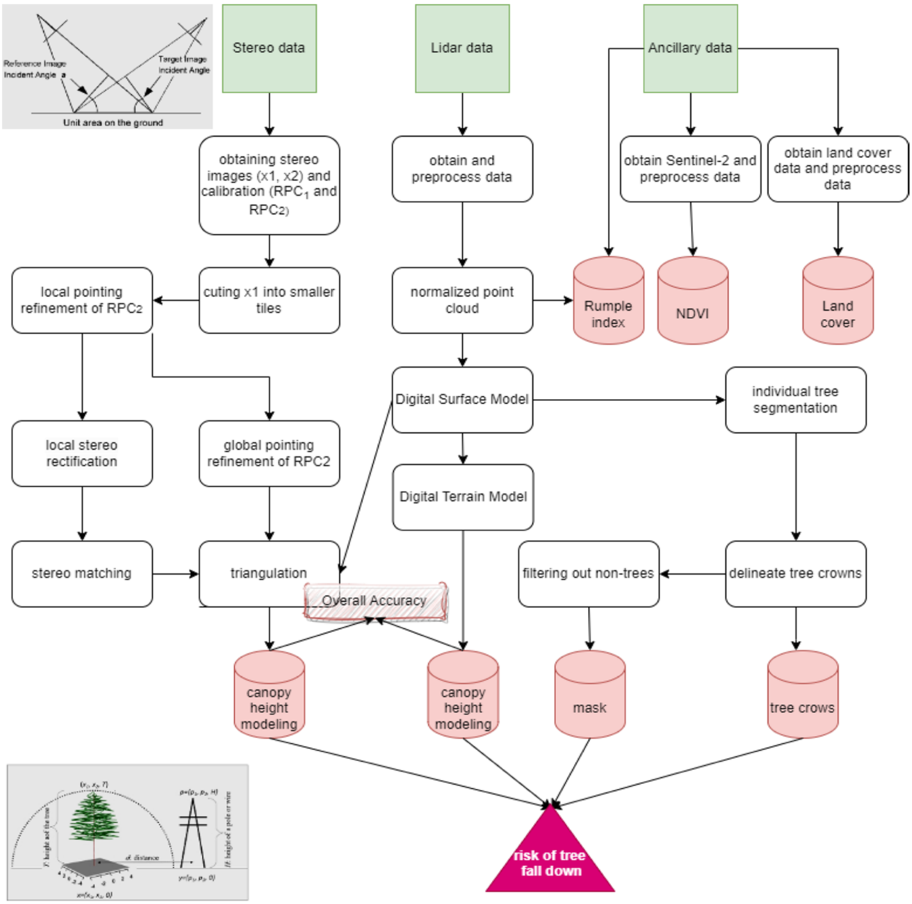

Fig. 1 Flow diagram depicting the key procedural steps employed in this study. We used stereo images obtained from optical satellites along with airborne LiDAR data to estimate canopy height and crown characteristics. Additionally, by integrating various data layers and methods, we calculate land cover, vegetation cover, and the Rumple Index. RPC refers to Rational Polynomial Coefficients. Ancillary data has been used to explain the findings of this study

and methods, we focused on land cover, vegetation cover, canopy height, tree crown characteristics, and canopy surface roughness of the canopy across the study sites to calculate the risks of tree falls (Sect. 2.4.4). Statistical analysis has been performed to compare the results of different study sites in Sect. 2.4.5.

2.2 Study sites

This project was funded by the European Space Agency and aimed to explore the potential of stereo images in monitoring tree fall risks. Due to data availability, we have selected two study sites in Finland that we call Site 1 and Site 2, and two study sites in Switzerland that we call Site 3 and Site 4 (Figs. 1A and 3A in Supplementary material). Table 1 shows the areas, extents, and mean slopes, based on Global Multi-resolution Terrain Elevation Data 2010 (GMTED2010) (Survey 2010). The Copernicus Global Land Cover Layers (CGLS-LC100) map for the period 2015–2019 at 100-m spatial resolution was used to analyze forest types across the study sites (Buchhorn et al. 2020). The CGLS-LC100 data shows the majority of forests in Site 1 and 2 are evergreen needle-leaf forests, whereas the majority of forests in Site 3 and 4 are deciduous broad-leaf and mixed forests (Fig. 4A).

2.3 Material

2.3.1 Pléiades stereo images

The Pléiades satellite constellation, comprising two identical satellites (Pléiades 1A and Pléiades 1B), provides very high-resolution optical images with a revisit interval of 24 h (User Guide, date of access: 04.09.2024). We used Pléiades to capture panchromatic images with a 70 cm nadir resolution and at a nominal resolution of 50 cm, covering a 20 km swath footprint. All Pléiades images in this study have been taken at the acquisition Mode PX. More information has been provided in Table 2.

2.3.2 Airborne LiDAR data

Airborne LiDAR data is used to obtain the three-dimensional structure of forests across the study site, with the potential to provide highly accurate and detailed measurements (Mallet and Bretar 2009; Wulder et al. 2008). The airborne LiDAR data of all four sites (LAS format, version 1.4) were processed with lastool and las2las tool (version 201003) (Isenburg 2014) and the R package *lidR* (version 4.0.3) (Roussel et al. 2020). The airborne LiDAR

Table 1 Site characteristics including area (ha), geographic coordinates (latitude and longitude in decimal degrees), and mean slope (°) for the study locations. Sites 1 and 2 are located in Finland, and Sites 3 and 4 are located in Switzerland

	Area (hectares)	Longitude (degree)	Latitude (degree)	Mean slope (degree)
Site 1	5.97	27.42–27.43	61.42 to 61.43	1.01
Site 2	6.66	27.37–27.37	61.45 to 61.45	2.38
Site 3	18.96	8.88–8.89	47.26 to 47.27	13.47
Site 4	20.87	8.97–8.98	47.26 to 47.27	7.20

Table 2 Stereo image acquisition details for Pléiades satellites in different study sites in Finland and Switzerland, including acquisition date, solar irradiance (W/m²/micrometer), solar azimuth (°), solar elevation (°), and along-track incidence angles (°). Sites 1 and 2 are located in Finland, and Sites 3 and 4 are located in Switzerland

	Acquisition date	Solar irradiance (watt/m^2/micrometer)	Solar azimuth (degree)	Solar elevation (degree)	Along the track incidence (degree)
Site 1 and 2 (Pléiades 1A)	2021-09-27 10:02:29.8	1540	180	26	19/17
Site 1 and 2 (Pléiades 1B)	2021-09-27 10:03:20.5	1540	180	26	20/− 10
Site 3 and 4 (Pléiades 1A)	2021-10-01 10:25:48.9	1549	164	38	− 8/9
Site 3 and 4 (Pléiades 1B)	2021-10-01 10:26:24.1	1549	164	38	− 7/9

dataset used in this study was obtained from associated Head Power companies in Finland and Switzerland and encompasses a point density of 105.76 pulses/m^2. The positional accuracy of the data is sub-meter with a scale factor of 0.01 applied to the X, Y, and Z coordinates. In the airborne LiDAR data of Sites 1 and 2, the coordinate reference system employed was ETRS89/EUREF_FIN_TM35FIN. In the airborne LiDAR data of Sites 3 and 4, the coordinate reference system employed in the data was CH1903 + /LV95.

2.3.3 Sentinel-2 and land cover data

We used 'Copernicus Sentinel data [2023]' to assess vegetation cover in our study sites. Sentinel-2 provides high-resolution, multi-spectral imaging data with a wide swath coverage, which provides data at a 10 m spatial resolution. Sentinel-2 Level-2A is atmospherically corrected using the Sen2Cor processor (version 2.5.5), by applying numerous atmospheric models, and measuring aerosol, and cloud masks.

We also utilized the ESA WorldCover 2021 product, which offers a high-resolution land cover map at a spatial resolution of 10 m on a global scale. ESA land cover data is calculated by the intergeneration of Sentinel-1 and Sentinel-2 datasets and includes 11 distinct land cover categories (Zanaga et al. 2022). The overall accuracy of the dataset is 76.7% by producing the dynamic yearly Copernicus Global Land Service Land Cover (CGLS-LC) (Buchhorn et al. 2020).

2.4 Method

2.4.1 Canopy height and tree crown estimation using airborne LiDAR

We performed the classification of the 3D point cloud data into the ground and non-ground points using the progressive morphological filter (Zhang et al. 2003). The acquisition and preprocessing of airborne LiDAR data were carried out in the *lidR* in R (Roussel et al. 2020). A crucial step in the preprocessing pipeline involved the generation of a Digital Terrain Model (DTM) through the application of the triangulation interpolation methods extracted from each study site (Roussel et al. 2020).

We calculated the Digital Surface Model (DSM), which represents the height of a surface by selecting the highest point within the DTM map (Popescu 2007; Ruiz et al. 2014). Point-to-raster algorithms were employed, involving the establishment of a grid with a one-meter resolution to detect the highest point within each grid cell and assign it to the corresponding pixel. We then calculated the height map by calculating the difference between DTM and DSM. To enhance the quality and completeness of the height map, we adopted a technique that involved replacing each point with a small circle of known diameter to simulate the footprint of laser beams. This approach increased the point cloud density and facilitated the smoothing of the height map (Baltsavias 1999; Roussel et al. 2020).

As this study focuses on the risk of trees for powerlines, we segmented individual trees to create a mask of tree no tree. To do that, we employed a watershed algorithm that involves treetops detection by utilizing a local maximum function in a variable window filter. This involved assigning the tag of a treetop to the highest cell within a circular window, where the size was dynamically adjusted based on the height observations of the cell at its center to segment individual trees (Pau et al. 2010; Vincent and Soille 1991). By progressively incorporating neighboring pixels surrounding each treetop into the corresponding tree object, we terminated the segmentation process when another tree or the background region was encountered.

2.4.2 Canopy height estimation using optical data

We employed S2P to calculate canopy heights in each study site using Pléiades images (de Franchis et al. 2014b). The S2P provides a robust result in comparison with other methods for generating 3D elevation models from high-resolution stereo images obtained from Earth observation satellites (Dandini et al. 2022; Gao et al. 2023). To accomplish canopy height estimation from the optical data, we initiated the process by partitioning the input images into smaller tiles. This division allowed us to process the images at a local host computer and approximate the push broom camera using an affine camera model. By doing so, we could simplify the search for corresponding points between each stereo image pair. Next, we refined the calibration data for each tile. This step involved correcting any biases present in the Rational Polynomial Coefficients (RPC) functions, which are used to model the cameras, as explained in the Pléiades Imagery User Guide. Pléiades stereo images are equipped with a pair of RPC functions that facilitate the conversion between image coordinates and geographic coordinates on the globe and allow for the mapping of three-dimensional points in object space to the image plane. In this projection, the 3D points are represented by their spheroidal coordinates in the World Geodetic System (WGS 84). By refining the calibration data, we ensured that the epipolar constraints derived from the camera parameters were as precise as possible. After calibrating the data, we performed stereo image rectification. This process involved adjusting the images to align the corresponding epipolar lines, which simplified the matching of points between stereo pairs. This step significantly improved the accuracy of the subsequent matching and reconstruction processes. For stereo matching, we used a standard algorithm to find correspondences between the rectified tile pairs. The algorithm determined the disparity between the images, which represents the difference in pixel coordinates of corresponding points. Finally, we combined the local refinements from all the processed tiles to compute a global correction of the calibration to identify the best possible continuity between the 3D points computed from different tiles to calculate DSM. As optical satellite data cannot penetrate forests directly for DTM creation, stereo image-based approaches are typically necessary to obtain a DTM from various sources, including the Shuttle Radar Topography Mission (SRTM) (Jarvis et al. 2008). Although such datasets are widely and freely available, they have been subjected to limitations in accuracy and resolution. Hence, to ensure a fair assessment of differences in canopy height estimation between airborne LiDAR and stereo methods (Goldbergs et al. 2019), we utilized an accurate DTM obtained from airborne LiDAR data as a consistent baseline to calculate height maps. The DTM represents the terrain elevation, excluding above-ground features such as vegetation and buildings, and remains relatively stable through time.

2.4.3 NDVI, land cover map, and Rumple Index

To ensure the quality of Sentinel-2 data, we applied mask pixels classified as cloud shadow, cloud, and thin cirrus with a threshold of 20 percent. Next, we used Sentinel-2 data red band (*Red*) and the near-infrared band (*NIR*) with a temporal resolution of 10 days between 2019-01-01 and 2022-01-01 for calculating NDVI (Eq. 1). The NDVI represents vegetation cover, ranging from − 1 to 1, where a value of − 1 indicates bare land while a value of 1 indicates dense vegetation cover. We used the mean function to present the map of the NDVI.

$$NDVI = \frac{NIR - Red}{NIR + Red} \tag{1}$$

We utilized the Rumple Index which evaluates information measuring the horizontal and vertical variation of canopy structure using the airborne LiDAR data (Nadkarni et al. 2004; Parker et al. 2004). The Rumple Index (m^2/m^2) is calculated by dividing the total surface area of the canopy (including any gaps present on the surface) by the ground surface area. To compute this index, we used airborne LiDAR data (Sect. 2.3.1) and employed a method outlined by Parker et al. (2004), which involved creating a three-dimensional triangular irregular network using the grid points of the canopy surface. The Rumple Index is then calculated by summing the areas of all the triangles formed with this approach and dividing it by the ground surface area at a 10 m spatial resolution as shown in Eq. (2):

$$\text{Rumple Index} = \frac{3D\ canopy\ surface\ model\ area}{ground\ area} \tag{2}$$

We used the NDVI, land cover map, and Rumple Index to explain the findings derived from the stereoscopy and height measurements using optical satellite data.

2.4.4 Identifying trees posing a potential danger

We developed a simple approach to identify trees posing potential danger in the vicinity of powerlines to address the main objectives of this study (Fig. 2, Fig. 6A). To this end, we used canopy height data from Sect. 2.4.1. and 2.4.2. and we calculated the nearest distance of each object to powerlines considering the heterogeneity of the area following (Van Etten and Hijmans 2010). We assume the following abstractions: The surrounding terrain of the powerlines is of constant height, which we without loss of generality choose to be *0*. A tree is equivalent to a tuple (x, T), the tree top position is denoted as $x = (x_1, x_2, 0) \in \mathbb{R}^3$ and the highest point of the tree is exactly $T \geq 0$ above it, i.e., its coordinates are (x_1, x_2, T). A powerline is equivalent to a tuple (a, b), with $a \in \mathbb{R}^3$ and $b \in \mathbb{R}^3$ so that the powerline is the line segment parallel to the ground from a to b, and its height is denoted as $H = a_3 = b_3$. If the line segment from a to

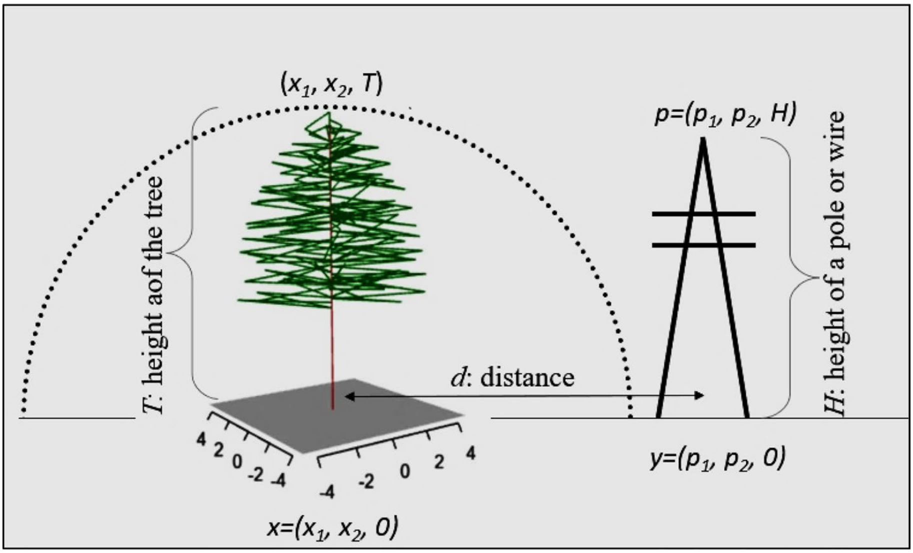

Fig. 2 Identification of potentially dangerous trees near powerlines using spatial configuration analysis. This image shows the affine 2-dimensional space S

b intersects the closed sphere with radius T and center x, we call (x, T) and (a, b) in dangerous configuration. Assuming that the line segment from a to b extends infinitely, then (x, T) and (a,b) are in a dangerous configuration if and only if the closest point $p=(p_1, p_2, H) \in \mathbb{R}^3$ on the line through a and b is an element of the closed sphere with radius T and center x. Let y be $(p_1, p_2, 0)$ and d the distance between x and y. We consider the affine 2-dimensional space S spanned by the affine basis x, p, and $(0, 0, 1)$. Then, (x, T) and (a, b) are in dangerous configuration if and only if p is an element of the closed circle of radius T with center x in S. Equivalently, $\sqrt{d^2 + H^2} \leq T$, which in turn is equivalent to $H \leq \sqrt{T^2 - d^2}$.

We used the canopy height (T) and shortest distance to a powerline (d) and use them to compute $F = \sqrt{T^2 - d^2}$. As the height of the powerline is known to be at least H', we consider all pixels with $F < H'$ as not dangerous. The remaining pixels are colored according to M meter bands, i.e., $H' + Mi \leq F < H' + M(i + 1)$ for $i \in \{0,1, \ldots\}$, representing increasing levels of risk. The results have been represented at 5 classes of lowest to highest risk of danger at 1-m spatial resolution.

We computed the Overall Accuracy (OA) as an evaluation metric for assessing the performance of stereo images in detecting dangerous trees. To evaluate the performance of the stereo images in detecting dangerous trees, we first constructed a contingency table (CT) by comparing the data obtained from the stereo image analysis with the airborne LiDAR data (Phillips 1995). Next, we calculated the OA as the ratio of the sum of correctly classified samples (SoCC) to the total number of samples (TNS) in the dataset multiplied by 100, according to the formula in Eq. (3):

$$QA = \frac{\sum \mathrm{SoCC}}{\sum TNS} * 100 \tag{3}$$

All the analyses in the Result Section are performed at pixel level, excluding QA estimation which is at tree level (Fig. 6A). We limited our investigation of tree fall potential to trees with a maximum height of 32-m, as measured by airborne LiDAR, due to the high uncertainties associated with the methods in this study for trees exceeding this height.

2.4.5 Statistical metrics

We used several statistical metrics to compare the performance of LiDAR and optical images in calculating mean values of canopy height at 1 m spatial resolution, which are outlined in this section.

We computed the mean (μ) as a central measure of the data distribution. The mean is calculated as the sum of all data points divided by the total number of observations as shown in Eq. (4):

$$\mu = \frac{1}{n}\sum_{i=1}^{n} x_i \tag{4}$$

We measure the standard deviation (SD), which quantifies the degree of variability or distribution within a dataset relative to the mean of the same data. The SD is derived from the variance, as demonstrated in Eq. (5)

$$SD = \sqrt{\frac{1}{n-1}\sum_{i=1}^{n} (x_i - \mu)^2} \tag{5}$$

Skewness (SK) provides insights into the asymmetry of the distribution. It is calculated in Eq. (6):

$$SK = \frac{\frac{1}{n}\sum_{i=1}^{n} (x_i - \mu)^3}{\sqrt{\frac{1}{n}\sum_{i=1}^{n} (x_i - \mu)^2}} \tag{6}$$

The skewness value indicates the extent and direction of deviation from a symmetric distribution. A positive skewness indicates a longer tail on the right side of the distribution, while a negative skewness indicates a longer tail on the left side.

Kurtosis (K) similarly measures the shape of the distribution by assessing the presence of outliers or extreme values. It is calculated in Eq. (7):

$$K = \frac{\frac{1}{n}\sum_{i=1}^{n} (x_i - \mu)^4}{\left(\sqrt{\frac{1}{n}\sum_{i=1}^{n} (x_i - \mu)^2}\right)^4} \tag{7}$$

A positive kurtosis indicates a relatively peaked distribution, with more values concentrated around the mean and heavier tails compared to a normal distribution. Conversely, a negative kurtosis suggests a flatter distribution, with fewer values concentrated around the mean and lighter tails compared to a normal distribution.

Moreover, we computed the coefficient of variation (CV) as an additional measure of data variability. It provides a relative measure of variation independent of the scale of the data, so that larger values indicate greater variability, and allows for comparison and interpretation of variability across different datasets. It was calculated using Eq. (8):

$$CV = \frac{100 * SD}{\mu} \tag{8}$$

We used Cross-tabulation analysis, a statistical method to examine the relationship between two categorical variables, for comparing the risk of tree fall for powerlines measurements by airborne Lidar and stereo (Momeni et al. 2018).

3 Results

3.1 Forest structure characteristics

The airborne LiDAR- and stereo-based height estimation and the statistical analysis, including mean, maximum, minimum, median, standard deviation, coefficient of variation, kurtosis, and skewness were computed to explore the key characteristics of the forests in each study site (Tables 3 and 4, Figs. 3 and 4).

The airborne LiDAR-based height estimation (Table 3) showed the mean canopy heights, ranging from 7.71 m (Site 1) to 12.58 m (Site 3). The maximum canopy height of 32 m and the minimum height of around zero was observed (Table 3). The median height values spanned from 0.27 m (Site 4) to 12.05 m (Site 3). The relatively high height value variability within the forest stands was presented by standard deviations ranging from 7.69 m (Site 1) to 10.83 m (Site 3). Site 2 and Site 4 also displayed relatively high standard deviation values of 9.13 m and 8.37 m, respectively. The coefficient of variation ranged from 86.12% (Site 3) to 131.26% (Site 4). Site 1 and Site 2 also displayed notable variations with *CV* values of 99.84% and 93.82%, respectively. Site 4 exhibited the lowest kurtosis value of −1.50, and Site 3 displayed a kurtosis value of −1.34. Site 2 and Site 1 exhibited kurtosis values of −1.23 and −0.79. On the other hand, Site 3 displayed the lowest skewness value of −0.10. Site 1 and Site 4 exhibited similar skewness values of −0.07, while Site 2 showed skewness of −0.05.

Table 3 Statistical analyses of canopy height measurements using airborne LiDAR data for each site. The *SD* refers to standard division and the *CV* refers to the coefficient of variation. Sites 1 and 2 are located in Finland, and Sites 3 and 4, are located in Switzerland

	Mean (m)	Max (m)	Min (m)	Median (m)	*SD* (m)	*CV* (%)	Kurtosis	Skewness
Site 1	7.71	31.88	0	5.3	7.69	99.84	– 0.79	– 0.07
Site 2	9.74	32.00	0	6.15	9.13	93.82	– 1.23	– 0.05
Site 3	12.58	32.00	0	12.05	10.83	86.12	– 1.34	– 0.10
Site 4	8.42	32.00	0	0.27	8.37	131.26	– 1.50	– 0.07

Table 4 Statistical analyses of canopy height measurements using stereo images for each site. The *SD* refers to standard division and the *CV* refers to the coefficient. Sites 1 and 2 are located in Finland, and Sites 3 and 4, are located in Switzerland

	Mean (m)	Max (m)	Min (m)	Median (m)	*SD* (m)	*CV* (%)	Kurtosis	Skewness
Site 1	4.66	31.91	0	1.62	5.20	111.66	– 1.38	0.04
Site 2	10.14	31.04	0	12.66	7.47	73.62	– 1.38	– 0.01
Site 3	10.23	31.99	0	6.21	10.34	101.03	– 1.36	0.01
Site 4	5.36	31.99	0	1.25	8.97	167.19	– 1.43	0.02

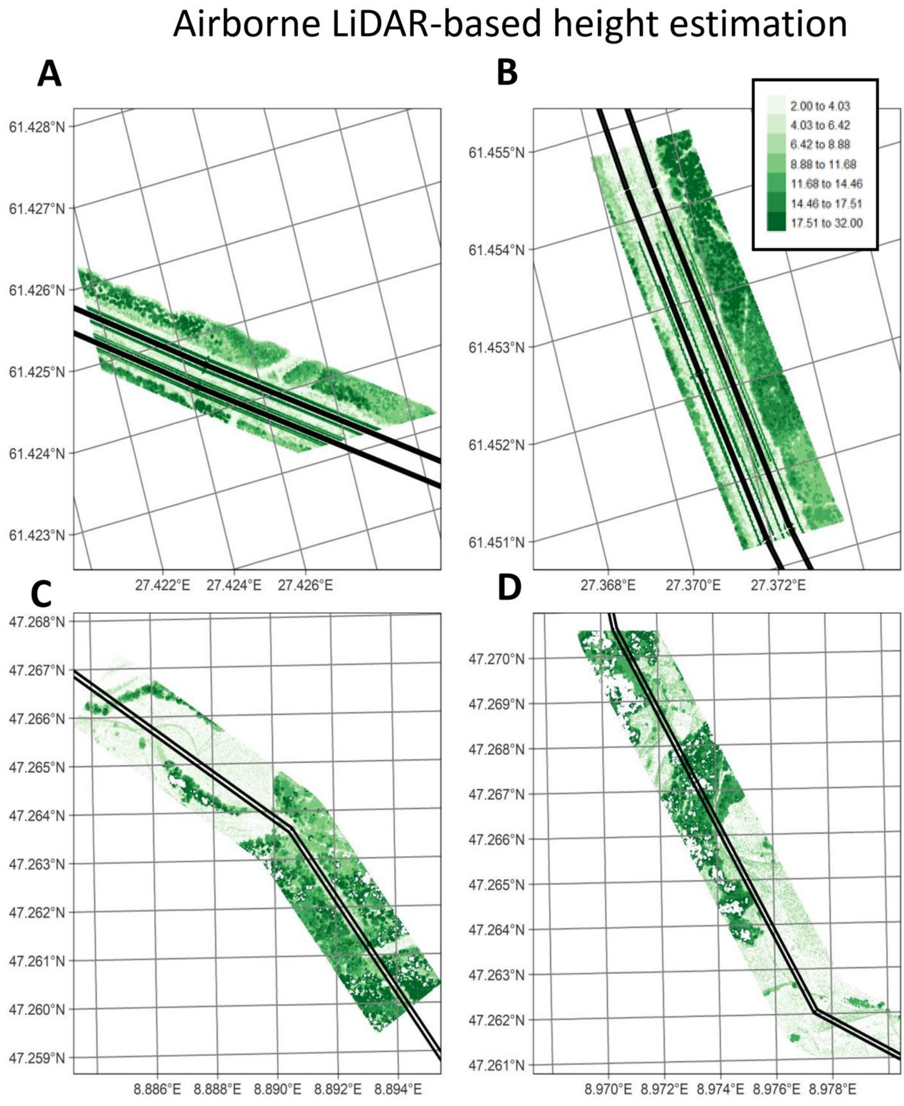

Fig. 3 Spatial variability of height map measurements using airborne LiDAR data. **A** and **B**, which are Sites 1 and 2, are located in Finland, and **C** and **D**, which are Sites 3 and 4, are located in Switzerland. The maps are generated with a 1 m spatial resolution using the Universal Transverse Mercator (UTM) coordinate system. The black lines represent powerlines

The stereo-based height measurements in Table 4 showed the mean canopy heights, ranging from 4.66 m (Site 1) to 10.23 m (Site 3). Site 2 exhibited a mean height of 10.14 m and Site 4 displayed the mean height of 5.36 m. The maximum height measurements obtained from stereo images aligned closely with the airborne LiDAR data, reaching around 32 m in all study sites. Similarly, the minimum height measurements from stereo images (Table 4) and airborne LiDAR (Table 3) both recorded values around zero. The median height values obtained from stereo images ranged from 1.25 m (Site 4) to

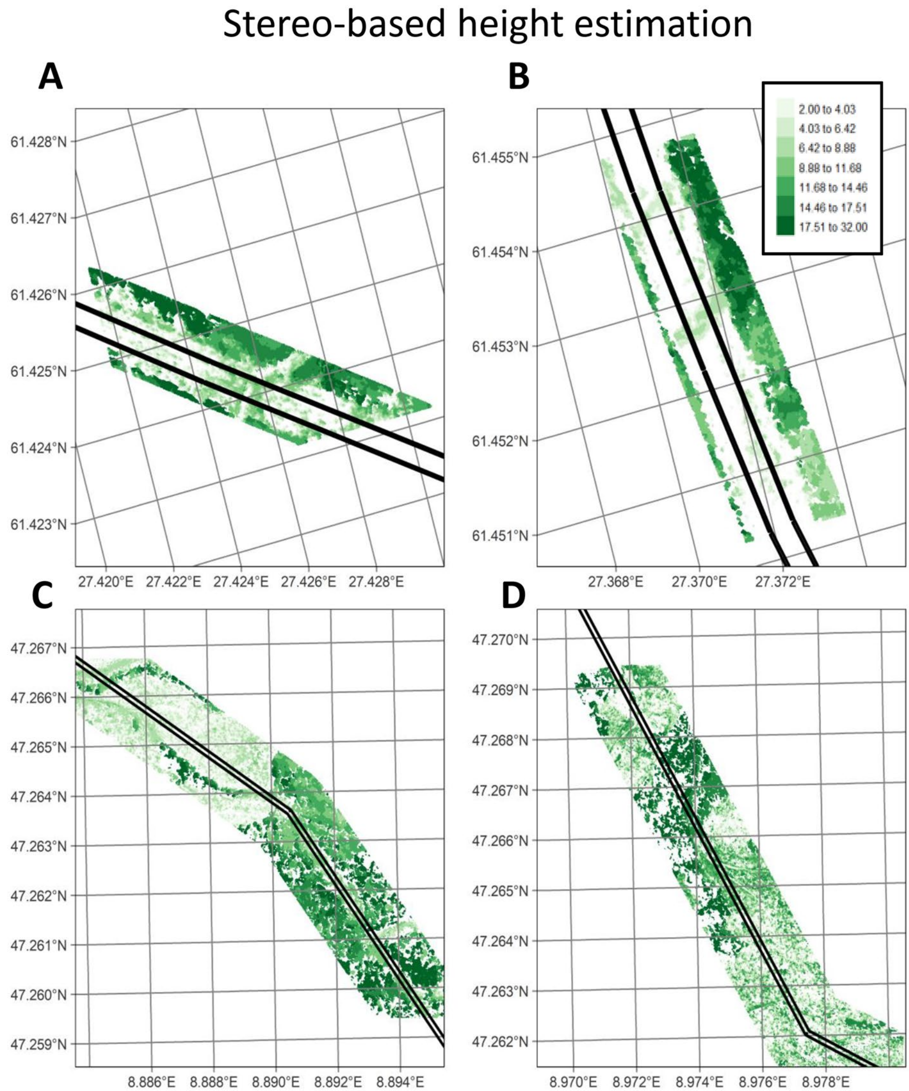

Fig. 4 Spatial variability of height map measurements using stereo images in meter units. **A** and **B**, which are Sites 1 and 2, are in Finland, and **C** and **D**, which are Sites 3 and 4, are in Switzerland. The maps are generated with a 1 m spatial resolution using the Universal Transverse Mercator (UTM) coordinate system. The black lines represent powerlines

12.66 m (Site 2), which was relatively similar to a range of median data observed in airborne LiDAR data (Table 3). The standard deviation values for stereo-based height measurements ranged from 5.20 m (Site 1) to 10.34 m (Site 3). As in Table 3, Site 3 displayed the highest standard deviation value of 10.34 m. The *CV* values obtained from stereo images analysis also exhibited a similar trend to the airborne LiDAR-derived *CV* values. Site 4 demonstrated the highest *CV* value of 167.19%, while Site 2 and Site 1 also displayed notable variations with *CV* values of 73.62% and 111.66%, respectively. Site 3 exhibited a relatively low *CV* value of 101.03% which aligned with its lower variability observed in the airborne LiDAR data. Kurtosis values from stereo images analysis also relatively matched with the airborne LiDAR results. More specifically, Site 4 exhibited the lowest kurtosis value of −1.43, while Site 3 displayed a kurtosis value of −1.36. Site 2 and Site 1 exhibited kurtosis values of −1.38 and −1.38. Regarding skewness values of stereo image analysis, all values were approximately close to zero by 0.04, −0.01, 0.01, and 0.02 in Site 1 to Site 4, respectively.

3.2 Land cover, NDVI, and Rumple Index

In this section, detailed information about the land cover type, NDVI, and Rumple Index for each study site was provided (Table 5, Fig. 5, and Fig. 5A of supplementary material). For Site 1, the land cover analysis revealed a predominant presence of forest. The mean NDVI value of this study site was 0.52. The mean Rumple Index value of 5.46 was obtained for Site 1, which corresponded to the horizontal and vertical variation of the canopy structure. The land cover analysis of Site 2 indicated the dominant presence of forests, similar to Site 1. The mean Rumple Index value of 7.68 was larger compared with Site 1. Site 3 exhibited a mosaic of forest and cropland classes. The land cover analysis revealed a moderate vegetation density that was indicated by a mean NDVI value of 0.73. The moderate mean Rumple Index value of 3.09 was significantly lower than the mean Rumple Index values in Site 1 and 2. Lastly, Site 4 presented a predominance of the forest and shrublands classes. The relatively high mean NDVI value of 0.71 indicated a relatively dense vegetation cover. The mean Rumple Index value of 2.54 was lower than other study sites (Alibakhshi 2020).

3.3 The risk of the tree falls using airborne LiDAR data versus stereo images

Table 5 provides a concise summary of the comparative analysis between airborne LiDAR and stereo-based height estimation. The coefficient of determination (R^2) values presented the strength of the relationship between height estimation via airborne LiDAR and stereo for all values in the extent of the study sites (Table 5 and Fig. 6). The R^2 values at Site 1 and Site 2 were 0.30 and 0.39, respectively. In contrast, the R^2 values at Site 3 and Site 4 were 0.64 and 0.62, respectively.

In addition to height estimation, the study assessed the mean NDVI and mean Rumple Index. Both Site 3 and Site 4 displayed higher mean NDVI values (0.73 and 0.71, respectively) compared to Site 1 and Site 2 (0.52 and 0.55, respectively). Regarding Rumple

Table 5 Summary of comparison between airborne LiDAR-based and stereo-based height estimation, as well as NDVI, and Rumple Index in each study site. The R^2 represents the strength of the relationship between airborne LiDAR- and stereo-based height estimation. Sites 1 and 2 are located in Finland, and Sites 3 and 4 are located in Switzerland

	Mean LiDAR	Mean stereo	R^2	Mean NDVI	Mean Rumple Index
Site 1	7.71	4.66	0.30	0.52	5.46
Site 2	9.74	10.14	0.39	0.55	7.68
Site 3	12.58	10.23	0.64	0.73	3.09
Site 4	8.42	5.36	0.62	0.71	2.54

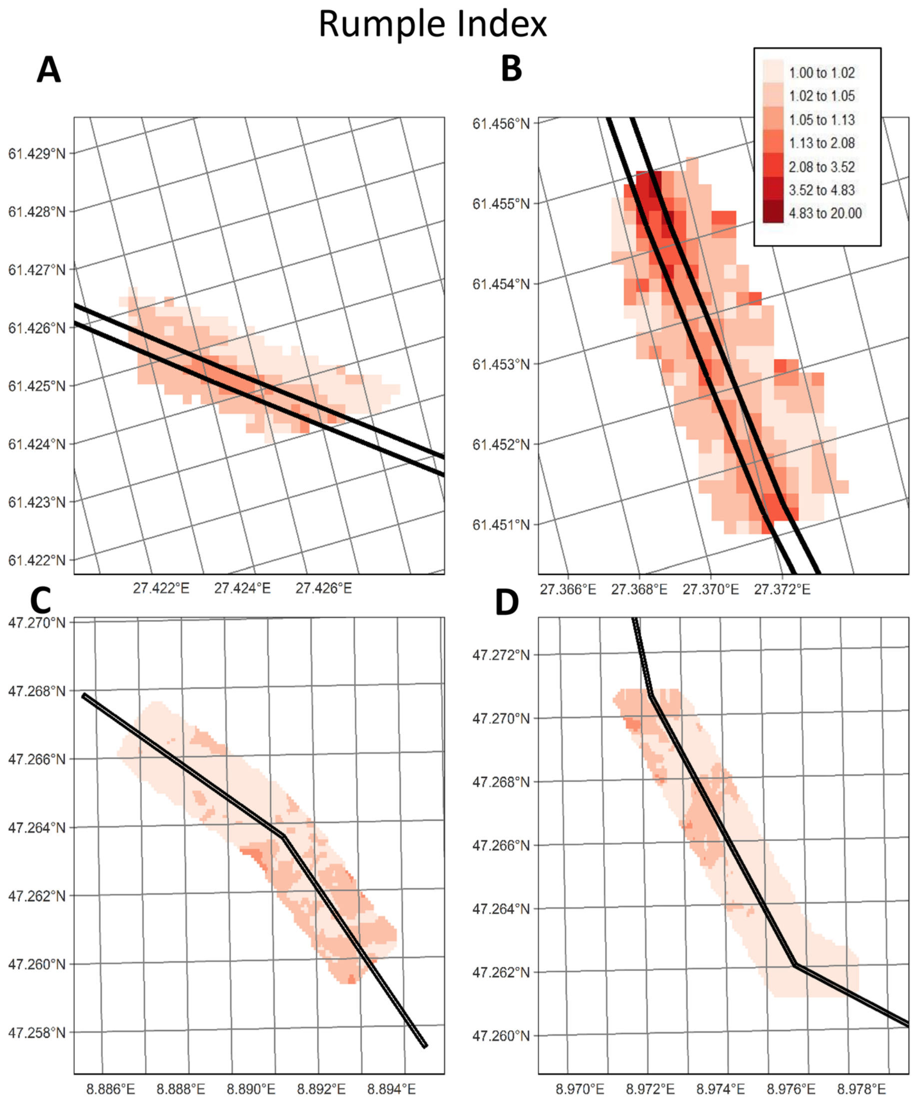

Fig. 5 Spatial variability of Rumple Index, ranging between 1 and 20, in each study site. **A** and **B**, which are Sites 1 and 2, are located in Finland, and **C** and **D**, which are Sites 3 and 4, are located in Switzerland. The maps are generated with a 10 m spatial resolution using the Universal Transverse Mercator (UTM) coordinate system. The black lines represent powerlines

Index values, Site 3 and Site 4 showed lower mean values (3.09 and 2.54, respectively) compared to Site 1 and Site 2 (5.46 and 7.68, respectively).

In addition to the quantitative analysis (Table 5), a bar plot was constructed to visually represent the relationship between airborne LiDAR measurements of forest height and the corresponding observations derived from stereo images (Fig. 7). The bar plot covered the entire range of airborne LiDAR measurements and suggests that, on average, stereo observations tended to increase as the height measurements obtained from airborne LiDAR

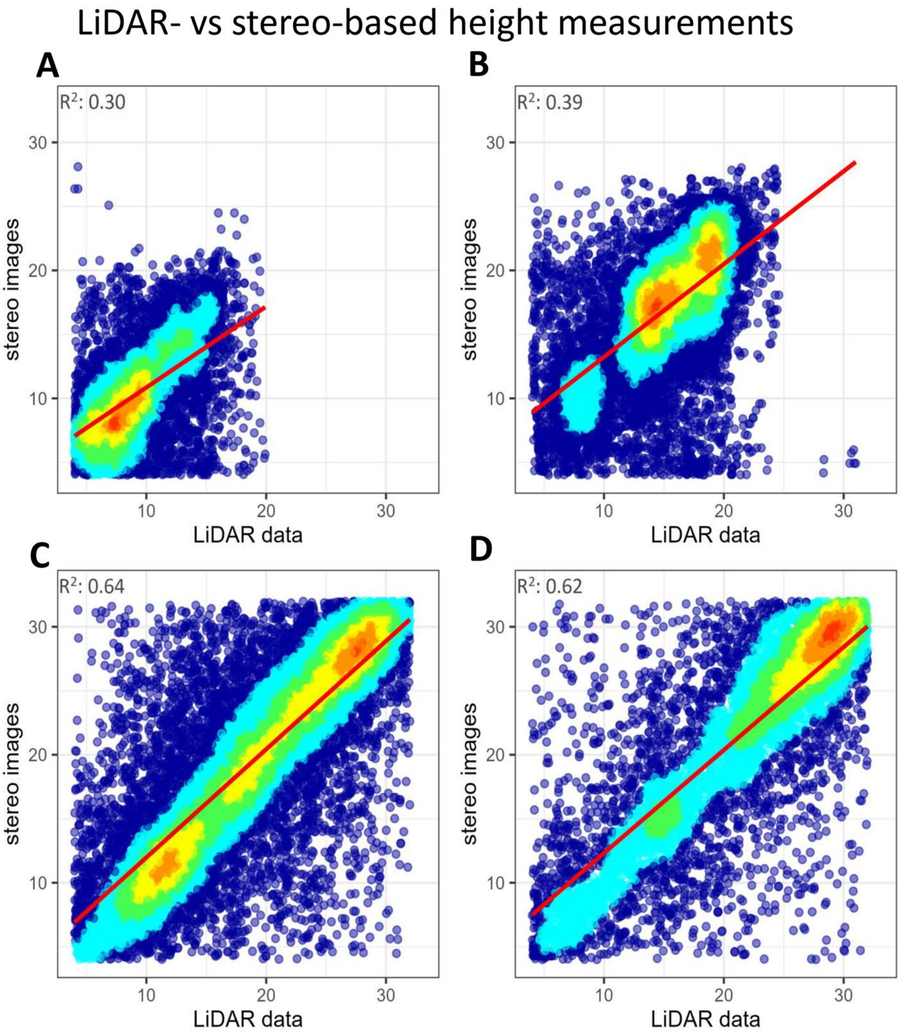

Fig. 6 Relationship between height map obtained from airborne LiDAR (x-axis) and stereo images (y-axis) in meter units. **A** and **B**, which are Sites 1 and 2, are in Finland, and **C** and **D**, which are Sites 3 and 4, are in Switzerland. Blue color refers to a lower density of points and red color refers to a higher density of points

increase. This may show that stereo-based analyses might have the ability to capture the overall patterns and variability in estimating canopy height. However, for values below 8 m, significant disagreements between the stereo observations and the corresponding airborne LiDAR measurements become apparent. These deviations were visually represented by notable differences in bar lengths or heights (Fig. 7).

Aiming to identify potential associations between the airborne LiDAR- and stereo-based measurements and the characteristics of the surface as represented by the Rumple Index, further analysis was conducted (Fig. 8). The best agreements between airborne LiDAR- and stereo-based height measurements were observed within a specific

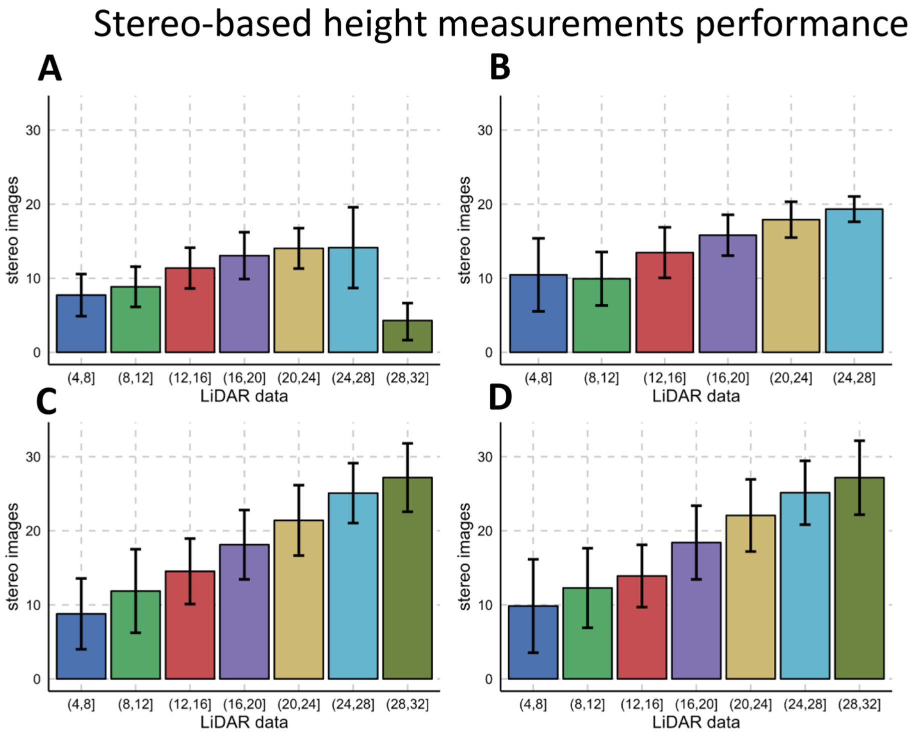

Fig. 7 Relationship between airborne LiDAR- vs stereo-based height estimation. **A** and **B**, which are Sites 1 and 2, are in Finland, and **C** and **D**, which are Sites 3 and 4, are in Switzerland. The plots show for each interval of airbone LiDAR-based height estimations, the mean value of stereo-based height estimations and the error bars designate the minimum and maximum values in these intervals

range of the Rumple Index, specifically between 1 and 3. Remarkably, Sites 3 and 4, which exhibited superior R^2 values also represent lower mean Rumple Index values (Fig. 7 and Table 5).

Following Sect. 2.4.4, we assessed the risk of tree falls by using cross-tabulation analysis between the detected dangerous trees using stereo images and airborne LiDAR data, categorizing them into five classes ranging from one (very high risk) to five (no risk). Our results (Fig. 9 and Fig. 10) demonstrated a significant level of agreement between the classifications derived from stereo images and airborne LiDAR data for the sites in Finland (Site A and B), as depicted in Fig. 9, with an estimated quality assurance of nearly 100% for the sites in Finland. The sites in Finland underwent a clear-cutting of trees near the powerlines which may explain the absence of risky trees in the context of this study based on our measurements. Additionally, Site 3 and Site 4 exhibited an agreement level of 95.16% and 92.14%, respectively. Although the sites in Finland did not reveal any dangerous trees, we included the results in this study to address false positive detections, where trees not posing a risk are incorrectly identified as hazardous. Using Fig. 9 and Fig. 10, data availability of stereo-based measurements and airborne LiDAR-based measurements can be visually compared.

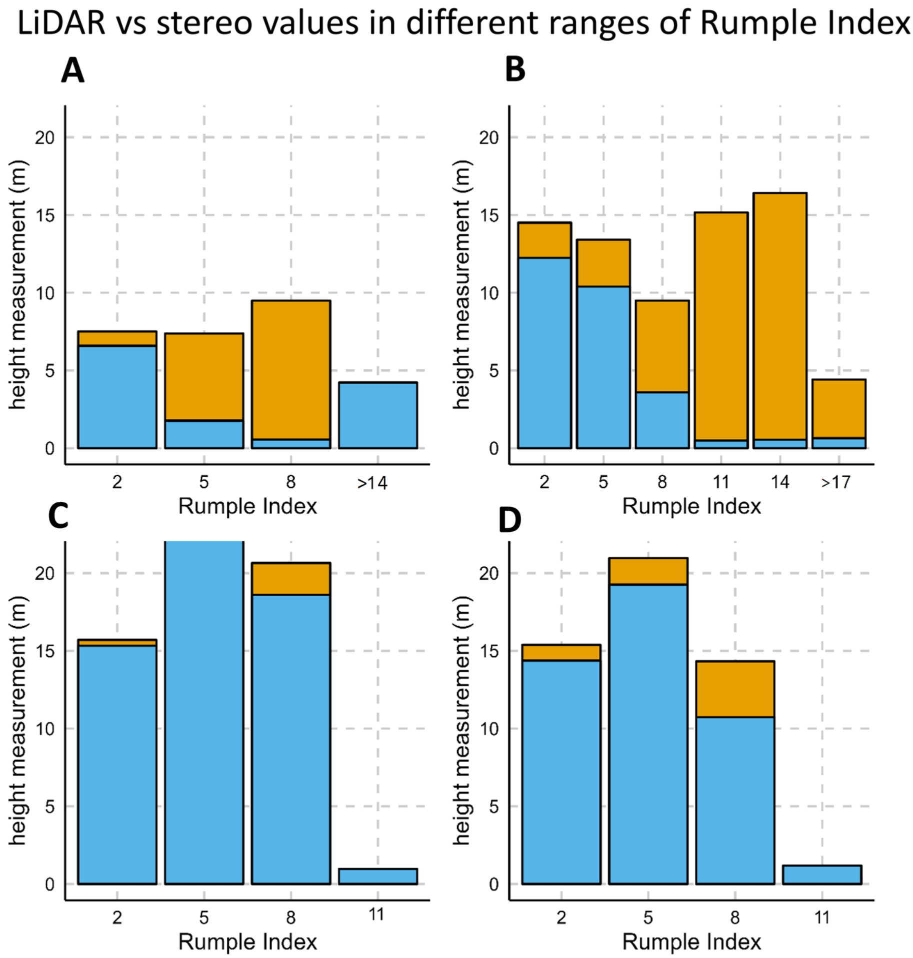

Fig. 8 Relationship between airborne LiDAR- vs stereo-based heigh estimation in a different range of Rumple Index (each value v on the x-axes stands for the interval (v−1, v+1];>v means (v, ∞)). **A** and **B**, which are Sites 1 and 2, are in Finland, and **C** and **D**, which are Sites 3 and 4, are in Switzerland. The blue color refers to height measurements using airborne LiDAR data and the orange color refers to height measurements using stereo images in different ranges of the Rumple Index

4 Discussion

We assessed the risk of tree fall-down for monitoring purposes, with a focus on calculating the accuracy of stereo-based height measurement in comparison with airborne LiDAR-based height measurement, as canopy height is an important parameter to calculate the tree fall risk potentials. The results revealed varying levels of accuracy between the stereo-based height estimations, and airborne LiDAR-based height estimations, where Sites 3 and Site 4 displayed relatively stronger correlations (R^2 = 0.64 and 0.62, respectively) compared with Site 1 and Site 2 (R^2 = 030 and 0.39, respectively) (Table 5). The lower mean Rumple Index values in Sites 3 and Site 4 (Table 5, Fig. 5)

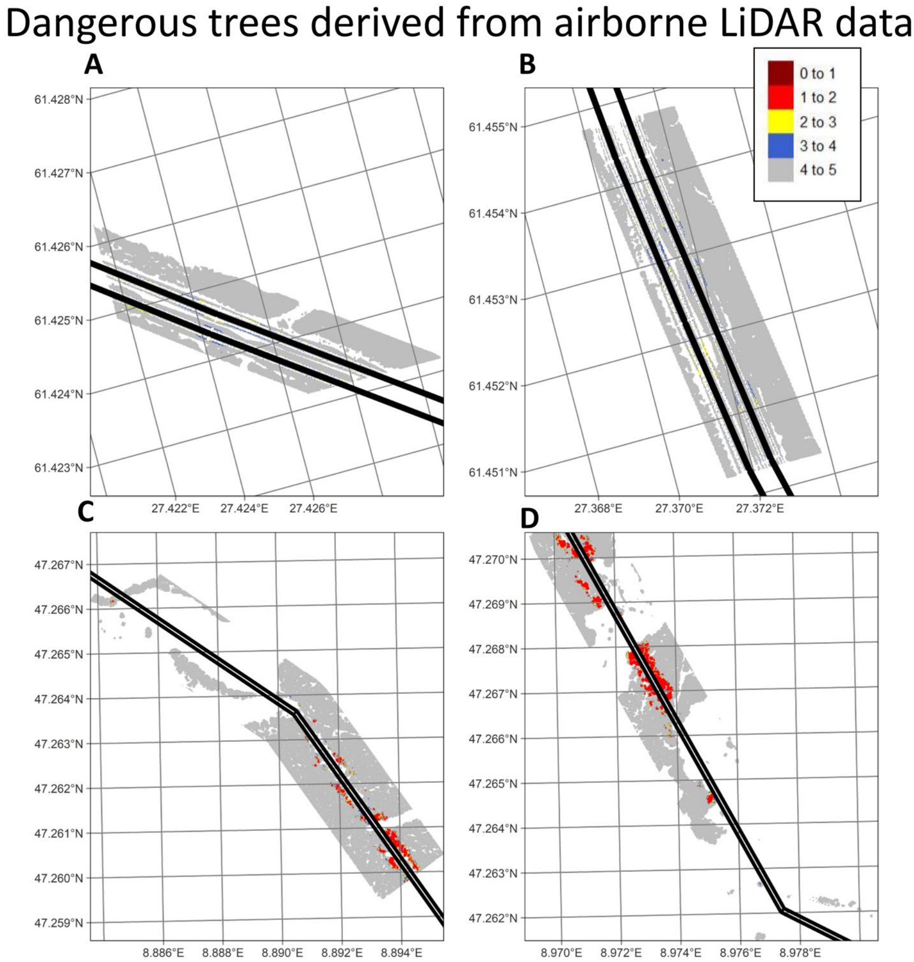

Fig. 9 Dangerous tree detection. **A** and **B**, which are Sites 1 and 2, are located in Finland, and **C** and **D**, which are Sites 3 and 4, are located in Switzerland. The maps are generated with a 1-meter spatial resolution using the UTM (Universal Transverse Mercator) coordinate reference system. The black lines represent powerlines. Class one represents very high risk and class five represents no risk

implied a relatively simpler and less complex surface compared to Site 1 and Site 2 (Table 5). As stereo techniques rely on distinctive features and matching algorithms that perform optimally in less complex environments (de Franchis et al. 2014c, 2014d), the reduced complexity in surface, presented by the Rumple Index in this study, can facilitate the performance of height measurements using optical satellite data. The Rumple Index presents the horizontal and vertical variation of the canopy structure (Nadkarni et al. 2004; Parker et al. 2004). Previous studies have reported Rumple Index can be controlled by forest type, forest structure, and biodiversity (Dayal et al. 2020; Fagua et al. 2021; Solano et al. 2022). Our study revealed that when the Rumple Index is approximately two, indicating a relatively simple canopy structure, stereo images yielded higher accuracy results (Fig. 8, Table 5). Kane et al. (2008) showed a surface with a Rumple Index around two can be classified as simple canopies. The cross-tabulation

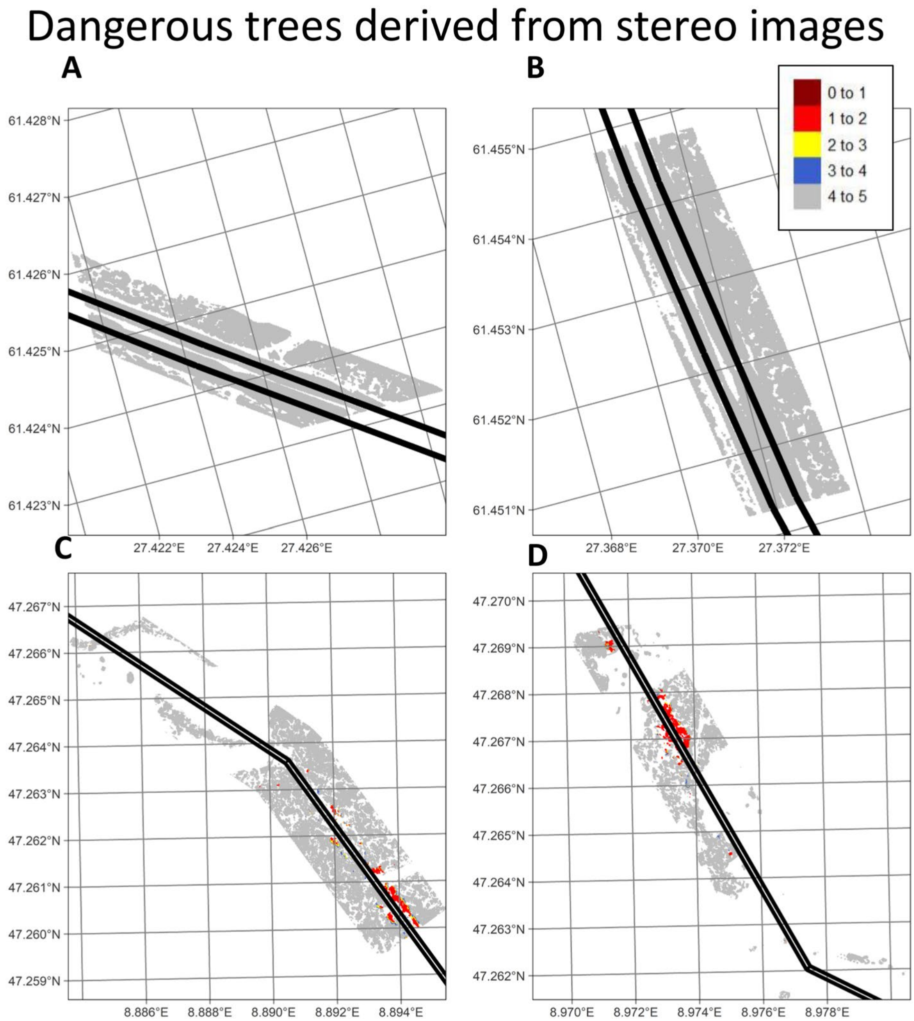

Fig. 10 Dangerous tree detection derived from stereo images. **A** and **B**, are Sites 1 and 2, which are located in located Finland, and **C** and **D**, are Sites 3 and 4, which are in located Switzerland. The layer has a 1-meter spatial resolution using the Universal Transverse Mercator (UTM) coordinate system. The black lines represent powerline. The class one represents very high risk and class five represents lowest risk

analysis (Fig. 9 and Fig. 10) showed a significant agreement between stereo image- and airborne LiDAR-based classifications for tree fall risk, particularly in simpler canopy environments. While the sites in Finland did not contain any dangerous trees due to prior clear-cutting near powerlines, their inclusion was critical for evaluating false positive detections. This ensures the method's robustness in identifying non-hazardous trees accurately. Sites 3 and 4 further demonstrated high agreement levels (95.16% and 92.14%, respectively). The data availability of stereo-based measurements and airborne LiDAR-based measurements can be visually compared, highlighting a potential source of uncertainty in stereo-based analyses (Fig. 9, Fig. 10).

The stereo-based height estimation results from our study (Tables 3 and 4) as well as results of previous studies, revealed a wide range of performance, from relatively weak (Lin et al. 2020; Persson et al. 2013; St-Onge et al. 2008; Ullah et al. 2020) to strong (Breaban et al. 2022; Tong et al. 2012; Ye et al. 2021). This variability in performance was largely influenced by the type of objects being measured. Studies focusing on buildings, that had simpler, well-defined structures, tended to achieve higher accuracy, consistently reporting errors of approximately one meter (Breaban et al. 2022; Tong et al. 2012; Ye et al. 2021; Zeng et al. 2014). However, when evaluating forest ecosystems that inherently had more complex surfaces (Lin et al. 2020; Persson et al. 2013; St-Onge et al. 2008; Ullah et al. 2020) than simple objects such as buildings, comparable accuracy levels to our study was reported (Tables 3 and 4). Specifically, in forested areas, the error in height estimation using stereo imagery can increase from 1.23 m in bare land to 4.24 m in more intricate ecosystems (St-Onge et al. 2008). It was reported that by excluding outliers, the R^2 value for height estimation improved from 0.53 to 0.91 when comparing airborne LiDAR and stereo imagery (St-Onge et al. 2008). Although removing outliers can significantly improve the R^2 values, considering the specific objective of monitoring dangerous trees in this study, every single tree should be counted in the risk assessment. Furthermore, previous studies reported varying R^2 values between 0.47 and 0.7 in different forests with different tree species (Hosseini et al. 2019; Wang et al. 2021), where the R^2 value in coniferous forests was higher than in deciduous forests. Needleleaf forests are typically characterized by dense, evergreen trees with needle-like leaves that often have a more uniform appearance compared with deciduous forests (Alibakhshi et al. 2020). The consistent structure and color of needle leaves forests may make it easier for stereo-matching algorithms to find correspondences between pixels. However, our results showed contrasting results, with lower R^2 values observed in coniferous forests in Finland compared to Switzerland. This discrepancy can be related to the presence of additional factors influencing the performance of stereo-matching algorithms such as variations in forest structure, canopy complexity, and environmental conditions (Sect. 2.4.2). This can again emphasize the importance of the Rumple Index in explaining the performance of stereo-based height measurement.

In this study, we initially obtained and analyzed SkySat stereo images to generate height maps, which provided stereo images with a spatial resolution of around 0.5 m. However, persistent errors in the images remained unresolved in the year 2021, despite our efforts in refining codes and requesting re-tasking from the Planet company. High uncertainty in the geolocation of the SkySat cameras and inconsistent orientation of individual scenes have been already reported (Bhushan et al. 2021; d'Angelo and Reinartz 2021), which could potentially explain the issues we encountered. As a result, we decided to exclude these images from the analysis, as their inclusion could introduce uncertainties and potential inaccuracies in our findings. Hence, we conclude the technology used in SkySat images is not still capable of being used in monitoring canopy height at least in our study sites.

Regarding the limitation of stereo imagery for height estimation, it should be noted that the algorithm (Sect. 2.4.2) requires a relatively coarse resolution of input to enable accurate matching of stereo image pairs in all study sites. This requirement arises from the need to identify corresponding features between the images. However, this enhanced resolution can lead to an increased occurrence of missing values in the resulting height calculation, when compared to the more comprehensive airborne LiDAR-based height measurement (Figs. 3 and 4). Furthermore, stereo imaging relies on the visibility of distinct features, and when the requirements are not fulfilled, it can result in height values with gaps or missing information. The presence of missing values implies that certain trees may not have their heights accurately estimated using the stereo imagery-based approach. Consequently, these missed trees could potentially pose risks or have the potential to cause damage, as their height and associated hazards may go unnoticed. In addition, the decreased resolution can lead to a loss of detail in the resulting height calculations. While we validated our stereo-based height measurements against airborne LiDAR data, we acknowledge that ground-truth data from field observations would provide a more rigorous accuracy assessment.

To enhance the accuracy of height estimation based on stereo imagery, several potential avenues warrant exploration. In our research, we made significant progress in this regard by incorporating an artificial neural network (ANN) approach, which resulted in notable improvements in the R^2 values. Specifically, our preliminary findings indicate that the R^2 values were enhanced to approximately 0.8 through the utilization of ANN techniques (detailed results to be published separately in a forthcoming manuscript). The integration of multi-source data, such as fusing stereo images with airborne LiDAR data or high-resolution optical imagery, holds promise for capturing complementary information and enhancing the accuracy of height mapping using stereo images. For example, the results (Table 5) highlight that NDVI can be one strong predictor that can enhance the potential for integrating multi-source data to improve height estimation accuracy. Additionally, advancements in image processing techniques, including improved stereo matching algorithms and robust DSM generation methods, can contribute to better height estimation.

It is important to emphasize that this study primarily focused on the development of an approach for measuring the risk of tree falls for powerlines. However, by assessing forest-related risks, the results can be further refined (Lee and Ham 2023; Pellikka and Järvenpää, 2003). For example, slender trees may tend to exhibit a higher susceptibility to falling. In addition, various environmental factors, such as snow or wind, and the type of tree play a pivotal role (Pellikka et al. 2000). Some species may be prone to experiencing crown snapping and some tree species may be prone to experiencing topple over with their root systems. By considering the time of the year (Molarius et al. 2014), forest type, and forest age, more comprehensive information on the risk of tree falls can be obtained. Regarding the limitation of this study, it should be noted that optical satellite data may cause complexities due to georeferencing, cloud, and shadowing effects and high error in estimating trees taller than 32-m, which limits the application of this study to when the highest quality satellite data are available (Fig. 9, Fig. 10). In addition, the model used in this study does not consider the line sag curve and assumes the lines are always the same height as powerlines throughout the year. To enhance the accuracy of our tree fall detection method, we recommend future studies focusing on incorporating additional contextual information beyond elevation changes. By combining elevation data with these additional layers of information, the classification model will become more robust, particularly in complex and heterogeneous forest environments.

Despite the advantages of direct height measurement provided by airborne LiDAR, it is important to acknowledge that stereo imagery still offers acceptable accuracy (mean 96.57%) in detecting risky trees, as demonstrated in our study (Sect. 3.3., Fig. 9). These findings align with a previous study that reported 98% accuracy (Ma et al. 2020). Our research adds knowledge to understanding stereo-based techniques and their potential for monitoring hazardous trees. By demonstrating the feasibility and effectiveness of stereo imagery along with the limitations in detecting risky trees, our study highlights the value of this approach as a cost-effective and accessible alternative to airborne LiDAR for tree hazard management and ensuring public safety.

5 Conclusion

This study highlighted the potential of very high-resolution optical satellite data as a valuable tool for tree fall risk monitoring and vegetation management. By comparing canopy height estimations derived from optical satellite data with those obtained from airborne LiDAR, we demonstrated the feasibility of using optical satellite data as a cost-effective alternative or complimentary data for monitoring tree fall risks for powerlines. The analysis of four study sites in Finland and Switzerland revealed varying levels of accuracy in height estimations, with stronger correlations observed in sites with lower Rumple Index values. An important takeaway from this study is the utility of the Rumple Index as a pre-assessment metric for selecting areas where stereo imagery can reliably substitute airborne LiDAR data. By identifying simpler canopy structures, the Rumple Index can help to optimize resource allocation for tree fall risk monitoring. However, the study also acknowledges the inherent limitations of stereo-based techniques, such as susceptibility to environmental factors like cloud cover and shadowing, as well as challenges in highly complex canopy environments. These findings emphasize the need for hybrid approaches that use both stereo imagery and airborne LiDAR data, depending on site-specific characteristics for comprehensive and accurate risk assessments. This balanced integration of technologies can offer an adaptable solution to meet the growing demands of vegetation management for infrastructure protection. This research contributes to a growing body of knowledge aimed at refining forest management practices by using high-resolution optical satellite data availability and actionable insights for enhancing the resilience of critical infrastructure against natural hazards.

Supplementary Information The online version contains supplementary material available at https://doi.org/10.1007/s11069-024-07016-y.

Author contributions All authors have contributed significantly to the research and approved the submission, and any funding or support received has been acknowledged.

Funding Open Access funding provided by University of Helsinki (including Helsinki University Central Hospital). Finnish Research Impact Foundation

Data availability Data are available as specified within the article or upon request. There are no conflicts of interest to declare.

Declarations

Conflict of interest The authors declare no conflicts of interest, financial or otherwise, that could have impacted the content or conclusions of this manuscript.

Ethical approval This manuscript is original, not previously published, nor under consideration elsewhere, and adheres to ethical research standards, including necessary approvals and consent where applicable

References

Ahmad J, Malik AS, Xia L, Ashikin N (2013) Vegetation encroachment monitoring for transmission lines right-of-ways: a survey. Electr Power Syst Res 95:339–352

Akbari H, Pomerantz M, Taha H (2001) Cool surfaces and shade trees to reduce energy use and improve air quality in urban areas. Solar Energy 70(3):295–310

Alibakhshi S, Naimi B, Hovi A, Crowther TW, Rautiainen M (2020) Quantitative analysis of the links between forest structure and land surface albedo on a global scale. Remote Sens Environ. https://doi.org/10.1016/j.rse.2020.111854

Alibakhshi S (2020) Remotely sensed monitoring of land surface albedo and ecosystem dynamics

Alvey AA (2006) Promoting and preserving biodiversity in the urban forest. Urban Forest Urban Green 5(4):195–201

Baltsavias EP (1999) Airborne laser scanning: basic relations and formulas. ISPRS J Photogramm Remote Sens 54(2–3):199–214

Bhushan S, Shean D, Alexandrov O, Henderson S (2021) Automated digital elevation model (DEM) generation from very-high-resolution planet SkySat triplet stereo and video imagery. ISPRS J Photogramm Remote Sens 173:151–165

Breaban A-I, Oniga V-E, Chirila C, Loghin A-M, Pfeifer N, Macovei M, Nicuta Precul A-M (2022) Proposed methodology for accuracy improvement of LOD1 3D building models created based on stereo pléiades satellite imagery. Remote Sens 14(24):6293

Brockerhoff EG, Barbaro L, Castagneyrol B, Forrester DI, Gardiner B, González-Olabarria JR, Lyver POB, Meurisse N, Oxbrough A, Taki H (2017) Forest biodiversity, ecosystem functioning and the provision of ecosystem services, vol 26. Springer, Berlin, pp 3005–3035

Buchhorn M, Lesiv M, Tsendbazar N-E, Herold M, Bertels L, Smets B (2020) Copernicus global land cover layers—collection 2. Remote Sens 12(6):1044

Dandini P, Cornet C, Binet R, Fenouil L, Holodovsky VY, Schechner Y, Ricard D, Rosenfeld D (2022) 3D cloud envelope and cloud development velocity from simulated CLOUD (C3IEL) stereo images. Atmos Measure Tech 15(20):6221–6242

Dayal K, Durrieu S, Alleaume S, Revers F, Larmanou E, Renaud J-P, Bouvier M (2020) Scan angle impact on LiDAR-derived metrics used in ABA models for prediction of forest stand characteristics: a grid based analysis. Int Arch Photogramm Remote Sens Spat Inf Sci 43:975–982

d'Angelo P, Reinartz P (2021) Digital elevation models from stereo, video and multi-view imagery captured by small satellites. Int Arch Photogramm Remote Sens Spat Inf Sci 43:77–82

De Franchis C, Meinhardt-Llopis E, Michel J, Morel J-M, Facciolo G (2014) An automatic and modular stereo pipeline for pushbroom images. ISPRS Ann Photogramm, Remote Sens Spat Inf Sci 3:49–56

de Franchis C, Meinhardt-Llopis E, Michel J, Morel J-M, Facciolo G (2014c) Automatic sensor orientation refinement of Pléiades stereo images. In 2014 IEEE geoscience and remote sensing symposium

de Franchis C, Meinhardt-Llopis E, Michel J, Morel J-M, Facciolo G (2014d) On stereo-rectification of pushbroom images. In 2014 IEEE international conference on image processing (ICIP)

Fagua JC, Jantz P, Burns P, Massey R, Buitrago JY, Saatchi S, Hakkenberg C, Goetz SJ (2021) Mapping tree diversity in the tropical forest region of Chocó-Colombia. Environ Res Lett 16(5):054024

Farmer R, Allen E (2006) Power system dynamic performance advancement from history of North American blackouts. In 2006 IEEE PES power systems conference and exposition

de Franchis C, Meinhardt-Llopis E, Michel J, Morel J-M, Facciolo G (2014) Automatic digital surface model generation from Pléiades stereo images. Rev Fr Photogramm Télédétect 208:137–142

Gao J, Liu J, Ji S (2023) A general deep learning based framework for 3D reconstruction from multi-view stereo satellite images. ISPRS J Photogramm Remote Sens 195:446–461

Goldbergs G, Maier SW, Levick SR, Edwards A (2019) Limitations of high resolution satellite stereo imagery for estimating canopy height in Australian tropical savannas. Int J Appl Earth Obs Geoinf 75:83–95

Guan H, Sun X, Su Y, Hu T, Wang H, Wang H, Peng C, Guo Q (2021) UAV-lidar aids automatic intelligent powerline inspection. Int J Electr Power Energy Syst 130:106987

Guggenmoos S (2003) Effects of tree mortality on power line security. J Arboric 29(4):181–196

Hobi ML, Ginzler C (2012) Accuracy assessment of digital surface models based on WorldView-2 and ADS80 stereo remote sensing data. Sensors 12(5):6347–6368

Hosseini Z, Naghavi H, Latifi H, Bakhtiari Bakhtiarvand S (2019) Estimating biomass and carbon sequestration of plantations around industrial areas using very high resolution stereo satellite imagery. iForest-Biogeosci Forest 12(6):533

Isenburg M (2014) LAStools—efficient lidar processing software (Version 140929), rapidlasso GmbH: Gilching. In Germany

Ituen I, Sohn G (2010) The way forward: advances in maintaining right-of-way of transmission lines. Geomatica 64(4):451–462
Ituen I, Sohn G, Jenkins A (2008) A case study: workflow analysis of powerline systems for risk management. Int Arch Photogramm, Remote Sens Spat Inf Sci 37(3B):331–336
Jarvis A, Guevara E, Reuter HI, Nelson AD (2008) Hole-filled SRTM for the globe : version 4 : data grid. In CGIAR consortium for spatial information. http://srtm.csi.cgiar.org/
Jinqiu W, Hanjun L, Jiakai Y, Yuhao C (2021) Tree barrier prediction of power lines based on tree height growth model. In IOP conference series: earth and environmental science
Kane VR, Gillespie AR, McGaughey R, Lutz JA, Ceder K, Franklin JF (2008) Interpretation and topographic compensation of conifer canopy self-shadowing. Remote Sens Environ 112(10):3820–3832
Lee S, Ham Y (2023) Measuring the distance between trees and power lines under wind loads to assess the heightened potential risk of wildfire. Remote Sens 15(6):1485
Lin X, Xu M, Cao C, Dang Y, Bashir B, Xie B, Huang Z (2020) Estimates of forest canopy height using a combination of ICESat-2/ATLAS data and stereo-photogrammetry. Remote Sens 12(21):3649
Loghin A-M, Otepka-Schremmer J, Pfeifer N (2020) Potential of pléiades and worldview-3 tri-stereo DSMs to represent heights of small isolated objects. Sensors 20(9):2695
Louit D, Pascual R, Banjevic D (2009) Optimal interval for major maintenance actions in electricity distribution networks. Int J Electr Power Energy Syst 31(7–8):396–401
Ma J, Cheng JC, Jiang F, Gan VJ, Wang M, Zhai C (2020) Real-time detection of wildfire risk caused by powerline vegetation faults using advanced machine learning techniques. Adv Eng Inform 44:101070
Mallet C, Bretar F (2009) Full-waveform topographic lidar: State-of-the-art. ISPRS J Photogramm Remote Sens 64(1):1–16
Molarius R, Tuomaala P, Piira K, Räikkönen M, Aubrecht C, Polese M, Zuccaro G, Pilli-Sihvola K, Rannat K (2014) Systemic vulnerability and resilience analysis of electric and transport network failure in cases of extreme winter storms. In: Beer M, Au SK, Hall JW (eds) Vulnerability, uncertainty, and risk: quantification, mitigation, and management. ASCE, Virginia, pp 608–617
Momeni A, Pincus M, Libien J, Momeni A, Pincus M, Libien J (2018) Cross tabulation and categorical data analysis. Introd Stat Methods Pathol. https://doi.org/10.1007/978-3-319-60543-2_5
Mooney H, Larigauderie A, Cesario M, Elmquist T, Hoegh-Guldberg O, Lavorel S, Mace GM, Palmer M, Scholes R, Yahara T (2009) Biodiversity, climate change, and ecosystem services. Current Opin Environ Sustain 1(1):46–54. https://doi.org/10.1016/j.cosust.2009.07.006
Mori AS, Lertzman KP, Gustafsson L (2017) Biodiversity and ecosystem services in forest ecosystems: a research agenda for applied forest ecology. J Appl Ecol 54(1):12–27
Nadkarni NM, Parker GG, Rinker HB, Jarzen DM (2004) The nature of forest canopies. Forest Canopies 1677:3–23
Parker GG, Harmon ME, Lefsky MA, Chen J, Pelt RV, Weis SB, Thomas SC, Winner WE, Shaw DC, Frankling JF (2004) Three-dimensional structure of an old-growth Pseudotsuga-Tsuga canopy and its implications for radiation balance, microclimate, and gas exchange. Ecosystems 7:440–453
Pau G, Fuchs F, Sklyar O, Boutros M, Huber W (2010) EBImage—an R package for image processing with applications to cellular phenotypes. Bioinformatics 26(7):979–981
Pellikka P, Seed ED, King DJ (2000) Modelling deciduous forest ice storm damage using aerial CIR imagery and hemispheric photography. Can J Remote Sens 26(5):394–405
Pellikka P, Järvenpää E (2003) Forest stand characteristics and wind and snow induced forest damage in boreal forest. In Proceedings of the international conference on wind effects on trees, held in September
Persson H, Wallerman J, Olsson H, Fransson JE (2013) Estimating forest biomass and height using optical stereo satellite data and a DTM from laser scanning data. Can J Remote Sens 39(3):251–262
Phillips GM (1995) Introduction to cross tabulation statistics for disparate impact cases. Litig Econ Digest 1(1):39–44
Piermattei L, Marty M, Karel W, Ressl C, Hollaus M, Ginzler C, Pfeifer N (2018) Impact of the acquisition geometry of very high-resolution Pléiades imagery on the accuracy of canopy height models over forested alpine regions. Remote Sens 10(10):1542
Popescu SC (2007) Estimating biomass of individual pine trees using airborne lidar. Biomass Bioenerg 31(9):646–655
Poulos H, Camp A (2011) Mapping threats to power line corridors for connecticut rights-of-way management. Environ Manage 47:230–238
Roussel J-R, Auty D, Coops NC, Tompalski P, Goodbody TR, Meador AS, Bourdon J-F, De Boissieu F, Achim A (2020) lidR: an R package for analysis of airborne laser scanning (ALS) data. Remote Sens Environ 251:112061

Ruiz LA, Hermosilla T, Mauro F, Godino M (2014) Analysis of the influence of plot size and LiDAR density on forest structure attribute estimates. Forests 5(5):936–951
Salas EAL (2021) Waveform LiDAR concepts and applications for potential vegetation phenology monitoring and modeling: a comprehensive review. Geo-Spat Inf Sci 24(2):179–200
Sittithumwat A, Soudi F, Tomsovic K (2004) Optimal allocation of distribution maintenance resources with limited information. Electr Power Syst Res 68(3):208–220
Solano F, Modica G, Pratico S, Box OF, Piovesan G (2022) Unveiling the complex canopy spatial structure of a Mediterranean old-growth beech (*Fagus sylvatica* L.) forest from UAV observations. Ecol Indic 138:108807
St-Onge B, Hu Y, Vega C (2008) Mapping the height and above-ground biomass of a mixed forest using lidar and stereo Ikonos images. Int J Remote Sens 29(5):1277–1294
Stone C, Webster M, Osborn J, Iqbal I (2016) Alternatives to LiDAR-derived canopy height models for softwood plantations: a review and example using photogrammetry. Aust for 79(4):271–282
Survey (2010) Courtesy of the US geological survey
Tong X, Hong Z, Liu S, Zhang X, Xie H, Li Z, Yang S, Wang W, Bao F (2012) Building-damage detection using pre-and post-seismic high-resolution satellite stereo imagery: A case study of the May 2008 Wenchuan earthquake. ISPRS J Photogramm Remote Sens 68:13–27
Ullah S, Dees M, Datta P, Adler P, Saeed T, Khan MS, Koch B (2020) Comparing the potential of stereo aerial photographs, stereo very high-resolution satellite images, and TanDEM-X for estimating forest height. Int J Remote Sens 41(18):6976–6992
Van Etten J, Hijmans RJ (2010) A geospatial modelling approach integrating archaeobotany and genetics to trace the origin and dispersal of domesticated plants. PLoS ONE 5(8):e12060
Vincent L, Soille P (1991) Watersheds in digital spaces: an efficient algorithm based on immersion simulations. IEEE Trans Pattern Anal Mach Intell 13(06):583–598
Wang J, Liu D, Quiring SM, Qin R (2023) Estimating canopy height change using machine learning by coupling WorldView-2 stereo imagery with Landsat-7 data. Int J Remote Sens 44(2):631–645
Wang Y, Zhang X, Guo Z (2021) Estimation of tree height and aboveground biomass of coniferous forests in North China using stereo ZY-3, multispectral Sentinel-2, and DEM data. Ecol Ind 126:107645
Wedagedara H, Witharana C, Fahey R, Cerrai D, Joshi D, Parent J (2023) Modeling the impact of local environmental variables on tree-related power outages along distribution powerlines. Electr Power Syst Res 221:109486
Wulder MA, Bater CW, Coops NC, Hilker T, White JC (2008) The role of LiDAR in sustainable forest management. For Chron 84(6):807–826
Ye J, Qiang Y, Zhang R, Liu X, Deng Y, Zhang J (2021) High-precision digital surface model extraction from satellite stereo images fused with ICESat-2 data. Remote Sens 14(1):142
Zanaga D, Van De Kerchove R, Daems D, De Keersmaecker W, Brockmann C, Kirches G, Wevers J, Cartus O, Santoro M, Fritz S (2022) ESA WorldCover 10 m 2021 v200
Zeng C, Wang J, Zhan W, Shi P, Gambles A (2014) An elevation difference model for building height extraction from stereo-image-derived DSMs. Int J Remote Sens 35(22):7614–7630
Zhang K, Chen S-C, Whitman D, Shyu M-L, Yan J, Zhang C (2003) A progressive morphological filter for removing nonground measurements from airborne LIDAR data. IEEE Trans Geosci Remote Sens 41(4):872–882

Authors and Affiliations

Sara Alibakhshi[1] · Ruben Valbuena[2] · Daniel Heinlein[3] · Lauri Häme[4] · Petri Pellikka[1,5,6]

✉ Sara Alibakhshi
sara.alibakhshi@helsinki.fi

[1] Department of Geosciences and Geography, University of Helsinki, Helsinki, Finland

[2] Department of Forest Resource Management, Swedish University of Agricultural Sciences, Umeå, Sweden

[3] School of Research and Graduate Studies, Arcada University of Applied Sciences, Helsinki, Finland

[4] Terramonitor, Ilmalankatu 2A, 00240 Helsinki, Finland

[5] Institute of Atmospheric and Earth System Research, Faculty of Science, University of Helsinki, Helsinki, Finland

[6] State Key Laboratory for Information Engineering in Surveying, Mapping and Remote Sensing, Wuhan University, Wuhan 430079, China